Journal of Alloys and Compounds 505 (2010) 125–129

Contents lists available at ScienceDirect

Journal of Alloys and Compounds

journal homepage: www.elsevier.com/locate/jallcom

Review

Preparation and characterization of tin-doped spinel ferrite

Vitor Cezar B. Pegoretti[a], Paulo R.C. Couceiro[b], Cláudia M. Gonçalves[a], Maria de Fátima F. Lelis[c], José D. Fabris[a,*]

[a] Departamento de Química, ICEx, Universidade Federal de Minas Gerais, Campus–Pampulha, 31270-901 Belo Horizonte, MG, Brazil
[b] Departamento de Química, Instituto de Ciências Exatas, Universidade Federal do Amazonas, Campus–Coroado II, 69077-000 Manaus, AM, Brazil
[c] Departamento de Química, CCE, Universidade Federal do Espírito Santo, Campus–Goiabeiras, 29075-910 Vitória, ES, Brazil

ARTICLE INFO

Article history:
Received 5 April 2010
Received in revised form 1 June 2010
Accepted 8 June 2010
Available online 18 June 2010

Keywords:
Mössbauer
Supertransferred hyperfine field
Rietveld

ABSTRACT

The chemical preparation of a tin-doped spinel ferrite via the co-precipitation method rendered a sample containing 48.2 mass% Fe^{3+}, 11.8 mass% Fe^{2+} and 13.0 mass% Sn. Powder X-ray diffractometry data collected with synchrotron radiation source revealed the co-existence of two crystallographic phases: one with cubic (spatial group, $Fd3m$) spinel and other with trigonal–hexagonal ($R\bar{3}c$) structure. ^{57}Fe Mössbauer spectroscopy analysis confirmed the occurrence of two tin-doped phases, with relative spectral areas of 50.6% and 49.4%; deduced chemical structures of these two phases correspond to $(Fe^{3+}, Fe^{2+})_{2.44}Sn^{4+}_{0.43}\oplus_{0.13}O_4$ and α-$Fe^{3+}_{1.88}Sn^{4+}_{0.12}O_3$, ($\oplus$, cation vacancy), respectively. The measured value for saturation magnetization $\sigma = 30\,J\,T^{-1}\,kg^{-1}$ for this sample leads to a Sn^{4+}-ferrite with $\sigma = 60\,J\,T^{-1}\,kg^{-1}$. The magnetic hyperfine field detected with ^{119}Sn Mössbauer spectroscopy was interpreted as being due to a supertransferred magnetic moment from iron cations to Sn^{4+} in octahedral sites of these iron oxides lattices.

Contents

1. Introduction

Magnetite is an iron oxide with chemical composition corresponding to Fe_3O_4, and has an inverse spinel crystallographic structure, in which Fe^{3+} fills tetrahedral and equivalent proportions of Fe^{3+} and Fe^{2+} occupy octahedral coordination sites. It can be oxidized to hematite (α-Fe_2O_3) either directly or via an intermediate formation of maghemite (γ-Fe_2O_3; also a spinel ferrite). The chemical and crystallographic mechanisms by which the oxidation of Fe^{2+} to Fe^{3+} in magnetite (Fe_3O_4; cubic) leads to hematite (α-Fe_2O_3; rhombohedral hexagonal) or maghemite (γ-Fe_2O_3; cubic or tetragonal) are not enough clear so far. In natural conditions, purer and well-crystallized bulk magnetite is directly transformed to hematite [1,2], whereas the oxidation of Fe^{2+} in the crystalline structure of highly substituted, small-sized grains and less well-crystallized iron-rich spinels leads first to maghemite prior the final conversion to hematite [3–6]. The conversion rate of magnetite to hematite seems to be somehow influenced by the climate, which prevailed during the rock weathering on the soil formation process [7]. The same general trend that is observed for natural systems is also valid for synthetic magnetite prepared in the laboratory: nano-sized synthetic magnetite tends to be directly converted to magnetite whereas bulk magnetite is preferentially oxidized to maghemite; then to hematite. In a particle-size distributed magnetite sample it is commonly observed the occurrence of both nano-maghemite and hematite as oxidation products.

The wide applicability of doped Fe_3O_4 in electrical transformer cores [8], magnetic memory devices [9] and as heterogeneous catalysts [10,11] is well known. Doping Fe_3O_4, γ-Fe_2O_3 [12,13] or α-Fe_2O_3 [14–17] with tetravalent tin has attracted special attention as some magnetic, electrical and other physical properties of the doped oxides may be conveniently controlled and enhanced.

* Corresponding author. Tel.: +55 31 3409 5753.
E-mail address: jdfabris@ufmg.br (J.D. Fabris).

0925-8388/$ – see front matter © 2010 Elsevier B.V. All rights reserved.
doi:10.1016/j.jallcom.2010.06.058

Systems based on α-$Fe_{2-x}Sn_xO_3$ have also favorable technological properties in gas-detector sensors, particularly for monitoring methane and carbon monoxide levels in gas mixtures [16,18–20].

Berry and co-workers [21,22] showed, using extended X-ray absorption fine structure (EXAFS) data, that tin adopts octahedral symmetry in both $Fe_{3-x}Sn_xO_4$ and α-$Fe_{2-x}Sn_xO_3$ and, by ^{119}Sn Mössbauer spectroscopy, that the diamagnetic nuclei of Sn^{4+} may show a magnetic hyperfine structure due to supertransferrence of magnetic moment from the nearest neighboring magnetic iron ions.

In the present work, it is characterized in some detail the chemical and crystallographic structures of a synthetic magnetic material containing primarily a tin-doped spinel ferrite and some secondary (Sn, Fe)-oxide.

2. Experimental methods

Sn-doped ferrite samples were prepared by co-precipitation in aqueous solutions of Sn^{4+} ($SnCl_2{\cdot}2H_2O$) and Fe^{3+} ($FeCl_3{\cdot}6H_2O$) chlorides, at room temperature, with ammonium hydroxide. The precipitate was washed with ammonium acetate, dried and heat-treated in a N_2 atmosphere at 420 °C for 2 h, according to procedures described in Ref. [23]. The indexes on the sample labels $Sn_{x_i \geq 0}$ are according to the general symbolic Formula (I) and, for side-formed species, later identified as being a Formula (II) ($x_i = x_M$ or $x_H \geq 0$; ⊕ = cation vacancy) type:

$$Fe_{3-x_M-y_M}Sn_{x_M}\oplus_{y_M}O_4 \quad (I)$$

$$\alpha\text{-}Fe_{2-x_H-y_H}Sn_{x_H}\oplus_{y_H}O_3 \quad (II)$$

The tin-doped sample ($Sn_{x_i>0}$) was characterized for its chemical composition by conventional chemical analysis, but also with data from energy dispersive spectroscopy (EDS), powder X-ray diffraction (XRD) collected with synchrotron radiation source at the Brazilian National Laboratory of Synchrotron Light (LNLS; Campinas, São Paulo), and ^{57}Fe and ^{119}Sn Mössbauer spectroscopy. Results were compared with those for the non-doped synthetic magnetite (Sn_0). The XRD data were refined by the Rietveld method using the FULLPROF [24] computer program. The saturation magnetization (σ) values were obtained with a portable magnetometer [25], under a fixed magnetic field about 0.3 T produced by a permanent magnet in the Halbach configuration [26].

The ^{57}Fe Mössbauer spectra were recorded at 298 K with a conventional constant acceleration transmission setup and a Co^{57}/Rh source with a nominal activity of about 20 mCi. Samples were diluted with sucrose so as to obtain about 10 mg cm^{-2} Fe. All isomer shift values are quoted relative to that of α-Fe at room temperature. The ^{119}Sn Mössbauer spectra were also recorded at 298 and 110 K with the same previously prepared sample and transmission setup arrangement using a $Ca^{119}SnO_3$ source with a nominal activity of about 3 mCi. The ^{119}Sn-isomer shift values are given relative to that of the gamma-source.

The scanning electron micrographs were obtained using JEOL JSM-840 A equipment; the samples were recovered with a gold-sputtered thin film.

Measurements of X-ray Absorption Near-Edge Structure (XANES) were collected at the Sn L_3-edge (3929 eV) at room temperature and pressure, in the transmission mode at the D04B-XAS1 beamline of the Brazilian National Laboratory of Synchrotron Light (LNLS; Campinas, São Paulo), equipped with a Si(1 1 1) double crystal monochromator, calibrated to the Ti K-edge (4965 eV), using a Ti metal foil. The vertical beam was set to a 0.8 mm width. Spectra were recorded from 3910 to 3980 eV with 0.3 eV steps and 7 s per step and from 3980 to 4150 eV with 1.0 eV steps and 7 s per step.

3. Results and discussion

From the elemental chemical analysis, the prepared non-doped Sn_0 sample (Table 1) contained 72.3 mass% Fe, whereas the main composition of the tin-doped $Sn_{x_i>0}$ sample was 11 mass% Sn and 58.7 mass% Fe.

Table 1
Saturation magnetization and chemical composition of samples.

Sample	σ (J kg^{-1} T^{-1})	Content (mass%)			
		EDS[a]	Dichromatometry		
		Sn	Fe^{2+}	Fe^{3+}	Fe
Sn_0	83		18.9	53.4	72.3
$Sn_{x_i>0}$	30	11	11.5	47.2	58.7

[a] Energy dispersive spectroscopy: average value obtained by probing ten points on each sample.

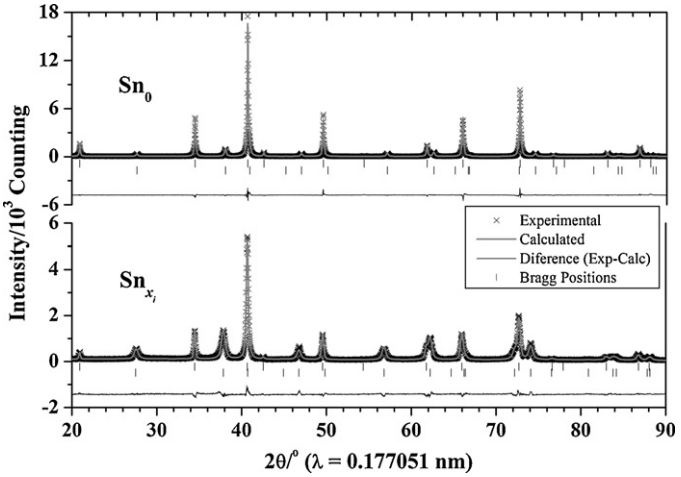

Fig. 1. Experimental and Rietveld-fitted powder X-ray patterns for samples Sn_0 and $Sn_{x_i>0}$.

The powder XRD (Fig. 1) for the Sn_0 sample actually indicates the co-existence of two iron oxides phases: one corresponding to magnetite (JCPDS [27] card # 19-629) and other to hematite (JCPDS card # 33-664). The ionic distribution obtained from the Rietveld refinement (Table 2) revealed that 14 mass% of the sample Sn_0 correspond to hematite, probably formed from the oxidation of spinel-structured iron oxide, and this explains the lower content of Fe^{2+} for the sample itself, relatively to that expected for a pure magnetite.

Similarly, two tin-doped iron oxides are identified for the sample $Sn_{x_i>0}$, corresponding to Formula (I) and Formula (II). No SnO_2 or other tin oxide was detected, confirming the virtually complete incorporation of tin atoms into the spinel and hematite crystallographic structures, as isomorphic substitutes, interstitial or other structural arrangements. R_{wp}, R_p, R_B, and R_f parameters obtained from the Rietveld refinement of X-ray diffraction patterns (Table 2) support the statistical confidence criterion of the fitting and the good estimation of these calculated profiles, confronted with the experimental patterns (Fig. 1).

The proportion of each phase from the Rietveld refinement (Table 2) is in good agreement with that deduced from ^{57}Fe Mössbauer data (Table 3), confirming the occurrence of two phases, in both samples. Saturation magnetization (σ) values corroborate this interpretation as a decrease in magnetization for the sample Sn_0, relatively to the pure Fe_3O_4, is assumed to be caused by the oxidation of $Fe^{2+} \rightarrow Fe^{3+}$ to form α-Fe_2O_3; a higher decrease in σ for the tin-doped sample $Sn_{x_i>0}$ may be explained as both oxidation of $Fe^{2+} \rightarrow Fe^{3+}$ in the spinel phase and structural incorporation of Sn (Table 1). The $(Fe^{3+}, Fe^{2+})_{3-x_M-y_M}Sn^{4+}_{x_M}\oplus_{y_M}O_4(x_M, y_M > 0)$ phase accounts for about 50% of the $Sn_{x_i>0}$ sample. This leads to a deduced saturation magnetization of $\sigma \approx 60$ J kg^{-1} T^{-1}, well below the corresponding value for the Sn_0 sample, $\sigma \approx 97$ J kg^{-1} T^{-1}, suggesting that $x_H, y_H \approx 0$, in the $\alpha\text{-}Fe^{3+}_{2-x_H-y_H}Sn^{4+}_{x_H}\oplus_{y_H}O_3$ structure.

The analysis of the XRD pattern (Fig. 1) shows broader reflections for the spinel phase of the $Sn_{x_i>0}$ sample than those for the non-doped sample, Sn_0. This broadening effect can be related to small-sized particles and eventually to some structural defects distribution in $(Fe^{3+}, Fe^{2+})_{3-x_M-y_M}Sn^{4+}_{x_M}\oplus_{y_M}O_4(x_M, y_M > 0)$. Indeed, the estimation of the average mean coherent length from the full width at half maximum (obtained from the Rietveld refinement using the Scherrer equation [28]) points to a smaller averaged particle size (Table 2) for the tin-doped ferrite, $(Fe^{3+}, Fe^{2+})_{3-x_M-y_M}Sn^{4+}_{x_M}\oplus_{y_M}O_4(x_M, y_M > 0)$. Also, the increase of the cubic lattice dimension (independently deduced from the

Table 2
Agreement factors for the Rietveld refinements (R_{wp}, R_p, R_B and R_f)[a] and refined parameters of XRD data. ⊕, cation vacancy. Number in brackets is the uncertainty estimated as standard deviation, expressed over the last significant digit of the fitted parameter value obtained from the least-squares algorithm.

Sample	Element content (mass%)	Space group	Chemical formula[b]	Lattice parameter (nm)	Phase content (mass%)	Cristallite size[c] (nm)	R_{wp}	R_p	R_B	R_f	Chi^2
Sn0	Fe_{total} = 72(1)	$Fd\bar{3}m$	Fe_3O_4	a = 0.83970(1)	86(1)	71(7)	10.3	7.68	1.94	2.75	2.34
		$R\bar{3}c$	Fe_2O_4	a = 0.50348(2) c = 1.37537(8)	14(1)	37(3)	10.3	7.68	3.66	2.93	2.34
$Sn_{x_i>0}$	Fe_{total} = 60(1) Sn_{total} = 13(1)	$Fd\bar{3}m$	$Fe_{2.44}Sn_{0.43}\oplus_{0.13}O_4$	a = 0.84015(3)	49(1)	71(6)	10.8	8.28	3.07	3.02	2.56
		$R\bar{3}c$	$Fe_{1.84}Sn_{0.12}\oplus_{0.04}O_3$	a = 0.50620(3) c = 1.3824(1)	51(1)	29(2)	10.8	8.28	4.56	4.03	2.56

[a] Agreement factors were calculated as follows: $R_{wp} = 100\left[\sum w_i(I_o - I_c)^2 / \sum w_i I_o^2\right]^{1/2}$; $R_p = 100\sum |I_o - I_c| / \sum I_o$; $R_B = 100\sum |I_{ko} - I_{kc}| / \sum I_{ko}$; $R_f = 100\sum |F_{ko} - F_{kc}| / \sum F_{ko}$; where I_o and I_c are the observed and calculated intensities; w_i is the weight assigned to each step intensity; I_{ko} and I_{kc} are the observed and calculated intensities for Bragg k-reflection; F_{ko} and F_{kc} are the observed and calculated structure factors.

[b] Chemical formula were estimated based on the Rietveld refinement of XRD data, Mössbauer and elemental chemical analysis; ⊕, cation vacancy; {} and [] denote tetrahedral and octahedral coordination sites, respectively.

[c] Average crystallite sizes were obtained from XRD data using the Scherrer equation.

Table 3
^{57}Fe Mössbauer parameters for Sn_0 and $Sn_{x_i>0}$ samples at 298 K. Numbers in brackets are uncertainties estimated as standard deviations, expressed over the last significant digit of the corresponding fitted parameter value obtained from the least-squares algorithm.

Sample	Assignment	δ (mm s^{-1})	ε (mm s^{-1})	B_{hf} (T)	Γ (mm s^{-1})	RA (%)
Sn_0	{$Fe^{2.5+}$}	0.662(3)	0.00(6)	45.76(2)	0.49(1)	51.9(3)
	[Fe^{3+}]	0.296(3)	−0.015(6)	48.76(2)	0.37(1)	34.8(2)
	Hm	0.353(9)	−0.14	50.50	0.47	13.3(3)
$Sn_{x_i>0}$	{$Fe^{2.5+}$}	0.593(3)	−0.04(1)	44.92(6)	0.37(2)	29.2(7)
	[Fe^{3+}]	0.333(4)	−0.043(8)	48.18(4)	0.38(1)	20.2(7)
	Hm	0.362(2)	−0.130(4)	49.76(2)	0.474(7)	50.6(6)

Rietveld structural refinement, Table 2) for this ferrite suggests that the isomorphical replacement of Fe^{3+} (ionic radium r = 65 pm [29]) by Sn^{4+} (r = 69 pm) does occur; any replacement of Fe^{2+} (r = 78 pm) by Sn^{4+} would tend to a decrease of the cubic lattice, according to Vegard's law [30].

The ionic charge balance can be obtained by replacing $3Sn^{4+}$ for $4Fe^{3+}$, creating a cation vacancy (⊕). The chemical formulae deduced from simultaneous charge and mass balances (Table 2) are $(Fe^{3+}, Fe^{2+})_{2.44}Sn^{4+}_{0.43}\oplus_{0.13}O_4$ and α-$Fe^{3+}_{1.88}Sn^{4+}_{0.12}O_3$, for the two phases. The ionic distribution obtained from the Rietveld structural refinement (Table 2) is in good agreement with these proposed formulae, so obtained from chemical data in Table 1.

The chemical structure for a stoichiometric and pure magnetite corresponds to $[Fe^{3+}]\{Fe^{2+}\ Fe^{3+}\}O_4$, where [] and {} denote tetrahedral and octahedral coordination sites, respectively. The fast electron hopping, which is known to be a pair-localized phenomenon in octahedral sites of magnetite, results in an electronic state corresponding to $Fe^{2.5+}$, yielding the following formula representation: $[Fe^{3+}]\{Fe^{2.5+}\}O_4$. The 298 K ^{57}Fe Mössbauer spectrum for the Sn_0 sample (Fig. 2) confirms the formation of iron-rich spinel phase as it shows two distinct sextets with hyperfine parameters (Table 3) assignable to Fe^{3+} in tetrahedral sites (sites A; hyperfine field, B_{hf} = 48.76(2) T; isomer shift relative to α-Fe, δ = 0.296(3) mm s^{-1}) and $Fe^{2.5+}$ in octahedral sites (sites B; B_{hf} = 45.76(2) T; δ = 0.662(3) mm s^{-1}), well in agreement with reported values in the literature (for instance, Ref. [31]). The relative subspectral area ratio (RA) between octahedral and tetrahedral sites occupancies (RA_B/RA_A = 51.9/34.8 = 1.49) confirms some oxidation $Fe^{2+} \rightarrow Fe^{3+}$ evidenced by the relatively smaller amount of Fe^{2+}, when compared with the expected value for a stoichiometric magnetite (RA_B/RA_A = 1.88). The hyperfine parameters for the other sextet are assignable to Fe^{3+} (B_{hf} = 50.50 T; δ = 0.353(9) mm s^{-1}) related to the deduced structure α-$Fe^{3+}_{1.88}Sn^{4+}_{0.12}O_3$.

The 298 K ^{57}Fe Mössbauer spectrum for the $Sn_{x_i>0}$ sample can be deconvoluted into three sextets (Fig. 2), two of them are assignable to iron in octahedral and tetrahedral sites of a typical spinel crystal structure; the third one is due to iron in hematite. The decrease of the isomer shift (δ = 0.593(3) mm s^{-1}), when compared with the expected value for iron in octahedral sites of the magnetite structure sustains the relatively low content of Fe^{2+} cations caused by some oxidation $Fe^{2+} \rightarrow Fe^{3+}$. Also, the decrease of the hyperfine field (B_{hf} = 44.92(6) T) may be due to the replacement of iron cations by Sn^{4+} ions. The decrease in the hyperfine field for hematite may be due to both small particle size and isomorphic substitution of Sn^{4+} for Fe^{3+}. The Sn^{4+} has d^{10} electronic configuration and no expected net magnetic moment. Moreover, the replacement of Fe for Sn in the octahedral sites explains the smaller areas ratio RA_B/RA_A = 29.2/20.2 = 1.45 (Table 3) between octahedral and tetrahedral sites occupancies than that of a pure magnetite.

^{119}Sn Mössbauer spectra, recorded for $Sn_{x_i>0}$ at both 110 and at 298 K can be resolved into three sextets and three doublets (Fig. 3). Even though the free Sn^{4+} ion has no magnetic moment, the probe-nucleus in this case senses a supertransferred magnetic hyperfine

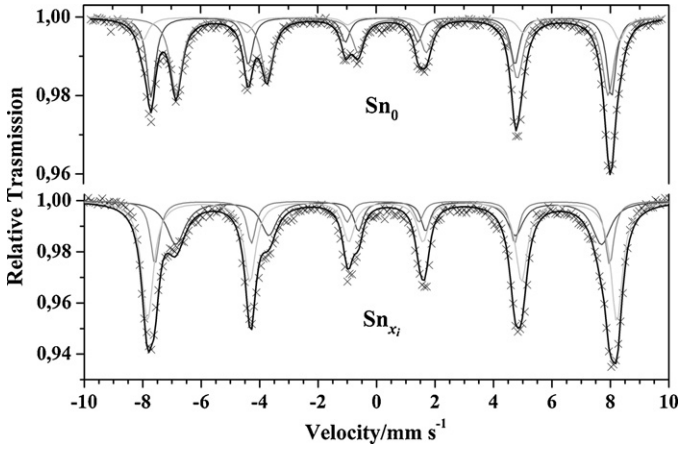

Fig. 2. ^{57}Fe Mössbauer spectra for the Sn_0 and $Sn_{x_i>0}$ samples at 298 K.

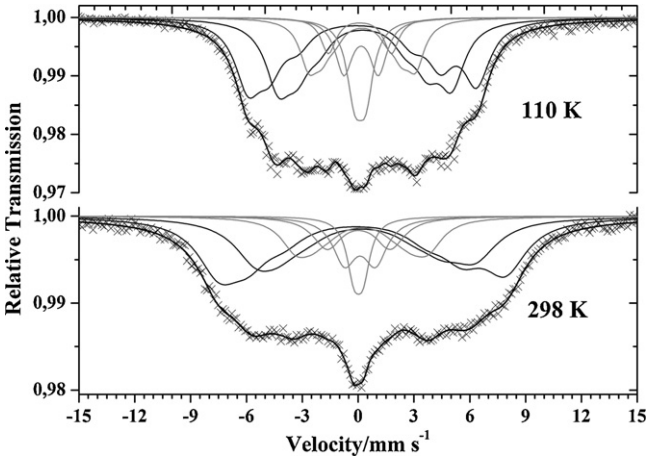

Fig. 3. ^{119}Sn Mössbauer spectra for the $Sn_{x_i>0}$ sample at 110 K and 298 K.

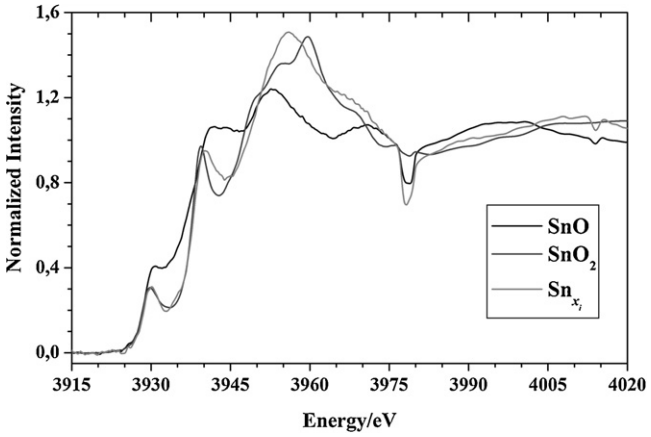

Fig. 4. XANES spectrum for the $Sn_{x_i>0}$ sample and standards SnO and SnO_2 at Sn L_3-edge.

field (STHI) from magnetic moments of iron ions in the spinel structure. The room temperature ^{119}Sn Mössbauer spectrum may be deconvoluted into three sextets, with hyperfine fields of 11.6(1), 8.9(2) and 5.4(2) T, that corresponds to 78% of the whole spectral area, and three doublets, corresponding to quadrupole splitting values of 0.49(8), 1.7(3) and 3.4(6) mm s^{-1} (Table 3). This set of results indicates that, as far as the hyperfine structure is concerned, the Sn^{4+} ions are not homogenously distributed in the spinel structure.

No SnO_2 reflection was identified on the XRD pattern. Thus, the three Mössbauer doublets (22% of the whole spectral area) can be due to either (i) a superparamagnetic relaxation or (ii) a very low magnetic hyperfine field contributions in this relatively broad linewidth multiple-spectrum pattern.

Mössbauer data collected at 110 K (Fig. 3) evidenced individual doublet splitting values corresponding to higher field gradients (Table 4) at the ^{119}Sn nucleus than those observed for the 298 K spectrum.

The XANES spectra for the Sn-ferrite sample and for the standard compounds are shown in Fig. 4. An apparently glitching signal appears at about 3980 eV but it may disregarded without compromising the confidence of the whole spectral analysis. The spectrum for the tin-doped sample compares well to that obtained for SnO_2

Table 4
^{19}Sn Mössbauer parameters at 110 K and 298 K for the $Sn_{x_i>0}$ sample. Numbers in brackets are uncertainties estimated as standard deviations, expressed over the last significant digit of the corresponding fitted parameter value obtained from the least-squares algorithm.

Temperature	Assignment	δ (mm s^{-1})	Δ, ε (mm s^{-1})	B_{hf} (T)	Γ (mm s^{-1})	RA (%)
110 K	Sextet 1	0.04(2)	0.54(4)	12.93(3)	2.43(5)	32(1)
	Sextet 2	0.42(2)	0.20(2)	9.82(3)	2.34(8)	30(1)
	Sextet 3	0.29(1)	0.03(2)	6.06(3)	1.61(9)	14(1)
	Doublet 1	0.16(1)	0.82(6)		1.4(2)	10(2)
	Doublet 2	0.23(2)	2.60(9)		1.6(2)	9(3)
	Doublet 3	0.14(2)	4.73(8)		1.4(2)	5(1)
298 K	Sextet 1	0.03(9)	0.4(2)	11.6(1)	2.8(2)	37(6)
	Sextet 2	0.3(1)	0.27(9)	8.9(2)	2.9(7)	27(8)
	Sextet 3	0.19(5)	0.02(9)	5.4(2)	1.91(6)	14(5)
	Doublet 1	0.02(4)	0.49(8)		0.9(3)	6(3)
	Doublet 2	0.10(5)	1.7(3)		1.5(9)	9(7)
	Doublet 3	0.03(6)	3.4(6)		1.9(8)	7(6)

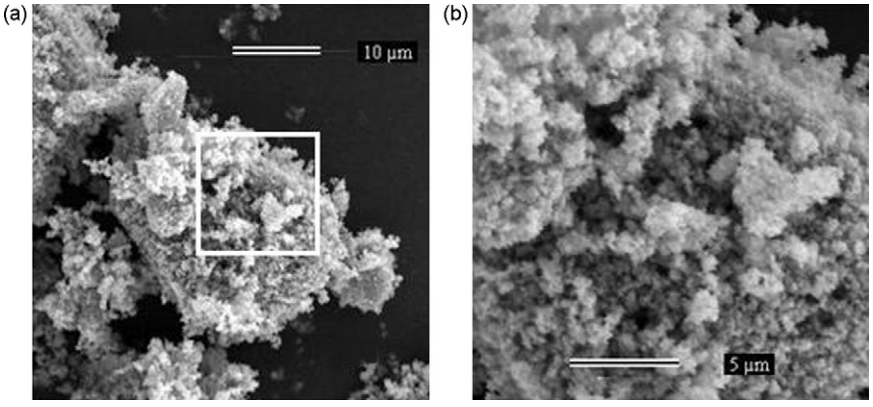

Fig. 5. Scanning electron micrographs of the Sn_0 sample: (a) magnified 2000×; (b) part of the sample equivalent to the portion marked with the squared area on the left-hand picture magnified 5000×.

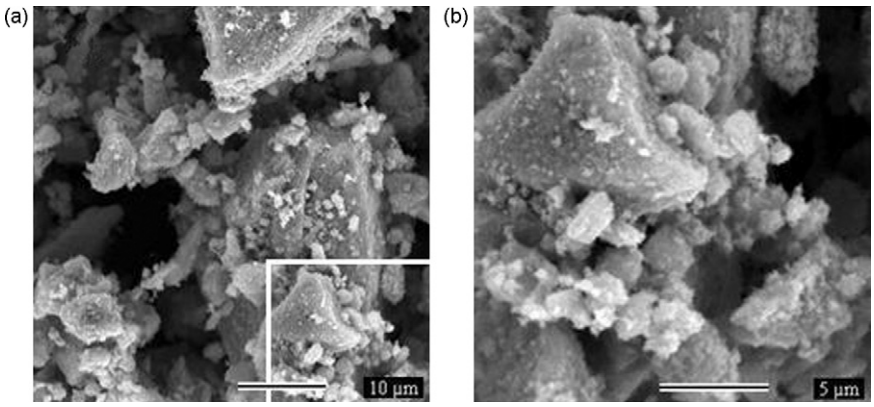

Fig. 6. Scanning electron micrographs of the $Sn_{x_i>0}$ sample: (a) magnified 2000×; (b) part of the sample equivalent to the portion marked with the squared area on the left-hand picture magnified 5000×.

rather than to the SnO standard. This, along with the ^{119}Sn Mössbauer isomer shift values (Table 4), indicates that tin is exclusively in the Sn^{4+} state in this ferrite structure.

Typical morphologies of the Sn_0 and $Sn_{x_i>0}$ particles are shown in Figs. 5 and 6, respectively. It can be observed that the spinel of sample Sn_0 tends to form more uniform agglomerates of small particles, whereas tin-doped ferrite of sample $Sn_{x_i>0}$ grows in octahedral habit.

4. Conclusion

In this work, a tin-doped spinel ferrite was prepared by the co-precipitation method but some partial oxidation led to a concomitant proportion of tin-doped hematite. The powder X-ray diffraction pattern evidenced an increase in the unit cell in both spinel- and corundum-related crystallographic phases of Sn-doped $(Fe^{3+}, Fe^{2+})_{2.44}Sn^{4+}_{0.43}\oplus_{0.13}O_4$ and α-$Fe^{3+}_{1.88}Sn^{4+}_{0.12}O_3$, relatively to the pure oxides, as it was obtained by the Rietveld refinement of XRD data. Moreover, ^{57}Fe Mössbauer data shows a decrease in the magnetic hyperfine field of the octahedral sites of this Sn-ferrite relatively to pure Fe_3O_4. The detection of supertransferred hyperfine fields at the ^{119}Sn probe-nucleus, by ^{119}Sn Mössbauer spectroscopy, confirms that the doping tin ions preferentially occupy octahedral sites of these Sn-doped spinel and corundum crystal structures, still below the solubility upper-limit of Sn in these oxides. The XANES and ^{119}Sn Mössbauer data point to both structures to be doped only by tin as Sn^{4+}.

Acknowledgements

Authors are indebted to Drs. Igor Vasconcelos (Federal University of Ceará, Brazil), Rogério Magalhães Paniago (Federal University of Minas Gerais, UFMG, Brazil) and Márcio César Pereira (UFMG). Work supported by FAPEMIG, CNPq, CAPES and Brazilian National Laboratory of Synchrotron Light (Brazil).

References

[1] G.P. Santana, J.D. Fabris, A.T. Goulart, D.P. Santana, Revista Brasileira de Ciência do Solo 25 (2001) 33–42.
[2] A.C. Doriguetto, N.G. Fernandes, A.I.C. Persiano, E. Nunes Filho, J.M. Grenèche, J.D. Fabris, Phys. Chem. Miner. 30 (2003) 249–255.
[3] M.C.F. Pinto, J.D. Fabris, A.T. Goulart, G.P. Santana, Hyperfine Interact. (C) 3 (1998) 325–327.
[4] J.D. Fabris, J.M.D. Coey, W. da, N. Mussel, Hyperfine Interact. 113 (1998) 249–258.
[5] A.T. Goulart, M.F. de Jesus Filho, J.D. Fabris, J.D.J.M.D. Coey, Phys. Chem. Miner. 25 (1) (1997) 63–69.
[6] J.D. Fabris, M.F. de Jesus Filho, J.M.D. Coey, W. da, N. Mussel, A.T. Goulart, Hyperfine Interact. 110 (1997) 23–32.
[7] A. Mijovilovich, H. Morras, C. Saragovi, G.P. Santana, J.D. Fabris, Hyperfine Interact. (C) 3 (1998) 332–335.
[8] J.D. Adam, S.V. Krishnaswamy, S.H. Talisa, K.C. Yoo, J. Magn. Magn. Mater. 83 (1990) 419.
[9] J.G. Lee, J.Y. Park, Y.J. Oh, C.S. Kim, J. Appl. Phys. 84 (5) (1998) 2801.
[10] S.C. Petrosius, R.S. Drago, V. Young, G.C. Grunewald, J. Am. Chem. Soc. 115 (1993) 6131.
[11] M.F.F. Lelis, A.O. Porto, C.M. Gonçalves, J.D. Fabris, J. Magn. Magn. Mater. 278 (2004) 263–269.
[12] Ö. Helgason, S. Steinthórsson, S. Mørup, Hyperfine Interact. 70 (1992) 985–988.
[13] N. Uekawa, M. Watanabe, K. Kaneko, F. Mizukami, J. Chem. Soc., Faraday Trans. 91 (1995) 2161–2166.
[14] P.B. Fabritchnyi, E.V. Lamykin, A.M. Babechkin, A.N. Nesmeianov, Solid State Commun. 11 (1972) 343–348.
[15] F. Schneider, K. Melzer, H. Mehner, G. Deke, Phys. Stat. Sol. A 39 (1977) K115.
[16] M. Takano, Y. Bando, N. Nakanishi, M. Sakai, H. Okinaka, J. Solid State Chem. 68 (1987) 153–162.
[17] S. Music, S. Popovic, M. Metikos-Hukovic, G. Gvozdic, J. Mater. Sci. Lett. 10 (1991) 197.
[18] H. Kanai, H. Mizutani, T. Tanaka, T. Funabiki, S. Yoshida, M. Takano, J. Mater. Chem. 2 (1992) 703–707.
[19] P. Bonzi, L.E. Depero, F. Parmigiani, C. Perego, G. Sberveglieri, G. Quattroni, J. Mater. Res. 9 (1994) 1250.
[20] Y. Liu, W. Zhu, M.S. Tse, S.Y. Shen, J. Mater. Sci. Lett. 14 (1995) 1185.
[21] F.J. Berry, Ö. Helgason, K. Jonsson, S.J. Skinner, Proc. Int. Conf. on Applications of Mössbauer Effect I, 1996, p. 59.
[22] F.J. Berry, S.J. Skinner, O. Helgason, R. Bilsborrow, J.F. Marco, Polyhedron 17 (1998) 149–152.
[23] P.P. de Abreu Filho, E.A. Pinheiro, F. Galembeck, L.C. Labaki, React. Solids 3 (1987) 241.
[24] J. Rodriguez-Carajal, 'FULLPROF' v.2.6.1 (ILL France), 1994; main based on the original code by R.A. Young, J. Appl. Crystallogr. 14 (1981) 149.
[25] J.M.D. Coey, O. Cugat, J. McCauley, J.D. Fabris, Revista de Física Aplicada e Instrumentação 7 (1992) 25.
[26] H.A. Leupold, I.E.E.E. Pontenziani, Trans. Magn. 23 (1991) 3628.
[27] Joint Committee on Powder Diffraction Standards (JCPDS), Mineral Powder Diffraction Files Data Book, International Center for Diffraction Data, Swarthmore, PA, 1980, p. 1168.
[28] H.P. Klüg, L.E. Alexander, X-ray Diffraction Procedures for Polycrystalline and Amorphous Materials, John Wiley & Sons, New York, 1974, 966 pp.
[29] G.W.C. Kaye, T.H. Laby, Tables of physical and chemical constants and some mathematical functions, 14th ed., Longman, London, 1975, p. 386.
[30] A.R. Denton, N.W. Ashcroft, Vegard's Law: Phys. Rev. A 43 (6) (1991) 3161.
[31] R.E. Vandenbergue, C.A. Barrero, G.M. da Costa, E. van San, E. de Grave, Hyperfine Interact. 126 (2000) 247–256.